

# Refractive-Index-Insensitive Nanolaminated SERS Substrates for Label-Free Raman Profiling and Classification of Living Cancer Cells

Wonil Nam,<sup>†</sup> Xiang Ren,<sup>†</sup> Seied Ali Safiabadi Tali,<sup>†</sup> Parham Ghassemi,<sup>†</sup> Inyoung Kim,<sup>‡</sup> Masoud Agah,<sup>†</sup> and Wei Zhou<sup>\*,†</sup>

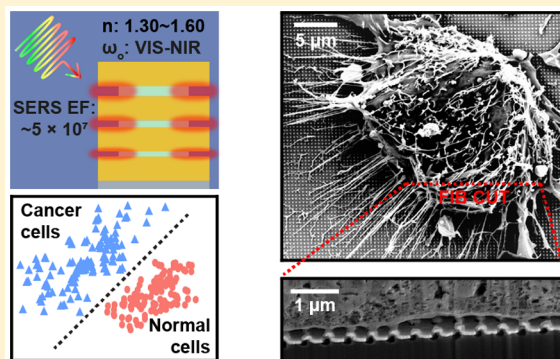
<sup>†</sup>Department of Electrical and Computer Engineering, Virginia Tech, Blacksburg, Virginia 24061, United States

<sup>‡</sup>Department of Statistics, Virginia Tech, Blacksburg, Virginia 24061, United States

**S** Supporting Information

**ABSTRACT:** Surface-enhanced Raman spectroscopy (SERS) has emerged as an ultrasensitive molecular-fingerprint-based technique for label-free biochemical analysis of biological systems. However, for conventional SERS substrates, SERS enhancement factors (EFs) strongly depend on background refractive index (RI), which prevents reliable spatiotemporal SERS analysis of living cells consisting of different extra-/intracellular organelles with a heterogeneous distribution of local RI values between 1.30 and 1.60. Here, we demonstrate that nanolaminated SERS substrates can support uniform arrays of vertically oriented nanogap hot spots with large SERS EFs ( $>10^7$ ) insensitive to background RI variations. Experimental and numerical studies reveal that the observed RI-insensitive SERS response is due to the broadband multiresonant optical properties of nanolaminated plasmonic nanostructures. As a proof-of-concept demonstration, we use RI-insensitive nanolaminated SERS substrates to achieve label-free Raman profiling and classification of living cancer cells with a high prediction accuracy of 96%. We envision that RI-insensitive high-performance nanolaminated SERS substrates can potentially enable label-free spatiotemporal biochemical analysis of living biological systems.

**KEYWORDS:** Surface-enhanced Raman spectroscopy (SERS), refractive-index-insensitive, nanolaminated, multiresonant plasmonics, Raman profiling, living cells, label-free



Surface-enhanced Raman spectroscopy (SERS) has emerged as a promising ultrasensitive molecular spectroscopy technique for biochemical analysis of living biological systems.<sup>1,2</sup> By surface plasmon mediated near-field enhancement of both optical excitation and inelastic Raman scattering processes of molecules in SERS hot spots of plasmonic nanostructures, the sensitivity of Raman spectroscopy can be increased by many orders of magnitude up to  $10^{11}$  with a detection limit down to the single-molecule level.<sup>2–4</sup> SERS bioanalytical strategies can be classified into label-mediated and label-free approaches.<sup>2,5,6</sup> For label-mediated SERS, the detection of molecules of interest is performed indirectly by monitoring SERS signals of surface-functionalized Raman reporter (or tag) molecules that specifically interact with the target molecule. Thus, label-mediated SERS provides excellent specificity in various intracellular and extracellular measurements.<sup>7–14</sup> Unlike label-mediated SERS, label-free SERS approaches directly measure intrinsic Raman signals of molecular ensembles present in hot spots without chemical modification and thus can allow for real-time label-free measurements and analysis of rich spectroscopic fingerprint profiles at subcellular scale in living biological systems.<sup>2,5,6</sup>

For direct label-free SERS analysis of living cells, SERS hot spots can be further categorized into two different forms, either in the unbound form as individual plasmonic nanostructures<sup>15–22</sup> or in the surface-bound form as dense arrays of plasmonic nanostructures on planar substrates.<sup>23–26</sup> For the unbound form, bottom-up synthesized plasmonic nanoparticles (NPs) have been successfully used in label-free SERS measurements of living cells to monitor the cellular transport pathway, local organelle environments, neurotransmitter release, and drug metabolism inside living cells.<sup>15–17,19,21,22</sup> However, label-free SERS analysis of living cells based on unbound plasmonic NPs still faces some challenges, such as (1) poor uniformity and reproducibility due to NP aggregation;<sup>2</sup> (2) limited chronic spatial controllability of SERS hot spots with regard to living cells due to the random diffusion and endolysosomal processes of NPs;<sup>2,5</sup> (3) challenge for long-term biological monitoring due to potential NP cytotoxicity.<sup>2,5,27,28</sup> As an alternate strategy to address these

**Received:** July 14, 2019

**Revised:** September 10, 2019

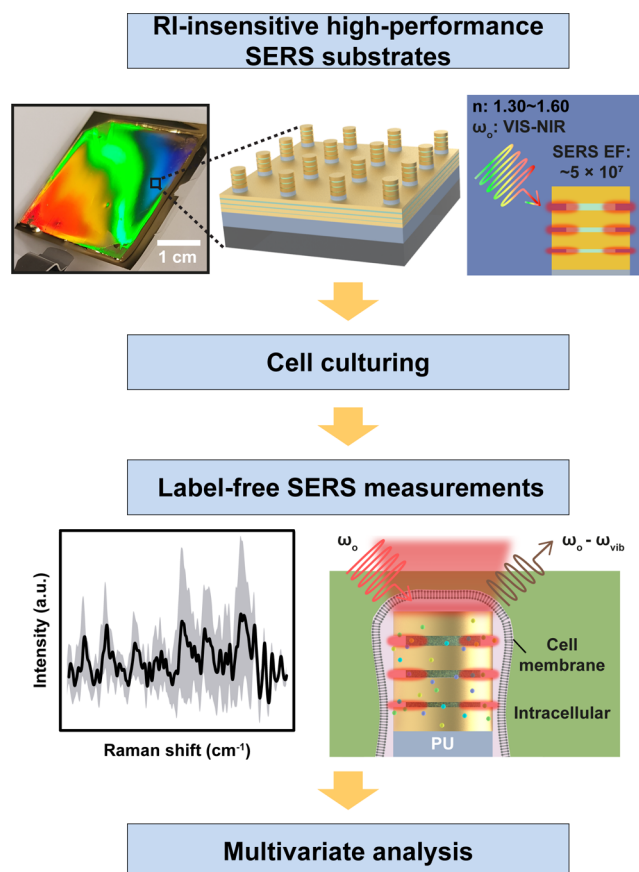
**Published:** September 16, 2019

issues, top-down fabricated SERS substrates with surface-bound plasmonic nanostructures have been recently used in label-free SERS measurements of living cells to differentiate living cancer cells and to monitor cell membrane dynamics upon electroporation.<sup>29,30</sup>

Despite the rapid progress in top-down nanofabrication of high-performance SERS substrates,<sup>31–34</sup> their widespread use in label-free SERS analysis of living cells is still prevented for several reasons, including poor fabrication scalability to produce large-area SERS substrates compatible with conventional cell culture studies, difficulty to generate optically dense and highly uniform arrays of hot spots required for quantitative spatiotemporal SERS analysis, and limited spectral control of nanogap plasmonic resonances in hot spots for SERS measurements with low phototoxicity and suppressed autofluorescence in the near-infrared (NIR) biological window. Moreover, another subtle but crucial issue for label-free living cell SERS is that the resonant wavelengths of plasmonic modes and associated SERS enhancement factors (EFs) in hot spots strongly depend on their local refractive index (RI) background of cells and cellular networks, where different intracellular and extracellular organelles/components can have different RI values ranging between 1.30 and 1.60.<sup>35,36</sup> Such a sensitive dependence of hot spot SERS EFs on large variations of local RI in biological systems will bias the relation between measured SERS signals and actual biomolecule concentrations detected in hot spots and make reliable spatiotemporal SERS analysis very difficult. Therefore, for label-free SERS measurements of living biological systems, it is highly desirable to achieve scalable fabrication of large-area RI-insensitive high-performance SERS substrates under NIR laser excitation.

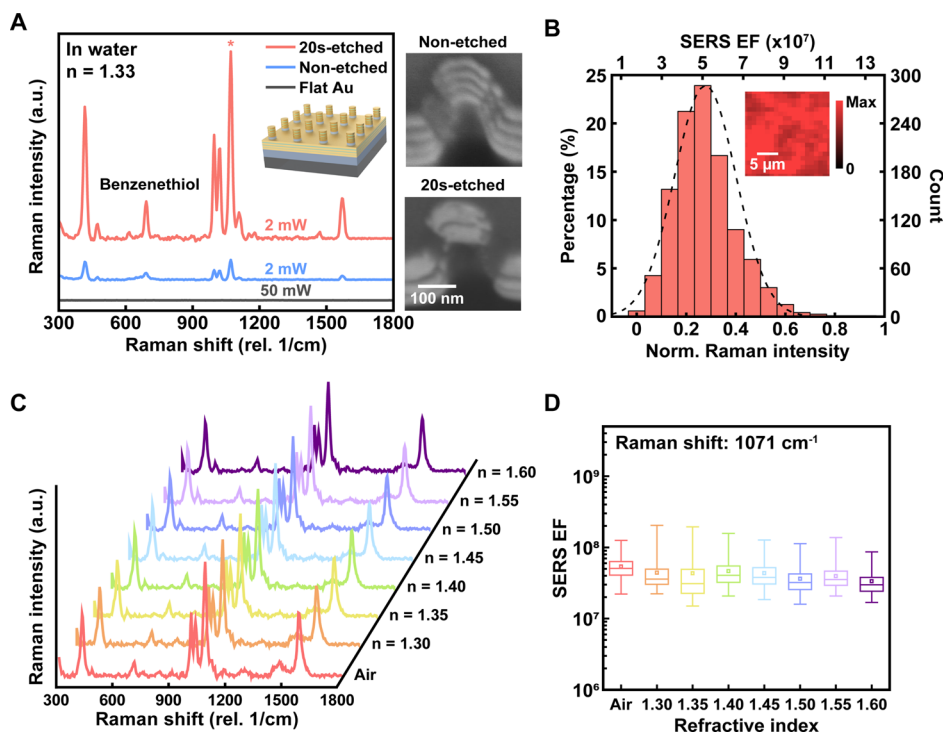
In this work, we report that nanolaminated SERS substrates based on multilayered metal–insulator–metal (MIM) plasmonic nanostructures can support optically dense and uniform hot spots with large SERS EFs ( $>10^7$ ) insensitive to background RI variations (1.30–1.60) and demonstrate their use for label-free SERS measurements and analysis of living breast cancer and breast normal cells. Measurements and numerical simulations of RI-dependent optical properties reveal that nanolaminated MIM plasmonic nanostructures can exhibit a RI-insensitive high-performance SERS response because they support a variety of hybridized plasmonic modes with spatial mode overlap and significant enhancement of local optical fields in nanogap regions across red and NIR range. Thus, compared to conventional SERS substrates, RI-insensitive multiresonant nanolaminated SERS substrates provide some unique opportunities for label-free SERS analysis of living cells. First, by providing optically dense and uniform hot spot arrays with large SERS EFs insensitive to background RI variations at subcellular scale, nanolaminated SERS substrates can potentially enable label-free SERS spatiotemporal mapping and analysis of complex biochemical activities in cells or cellular networks. Furthermore, the intrinsic multiresonant optical properties of nanolaminated SERS substrates can allow for wavelength-multiplexed multimodal operation by combining SERS with other optical sensing or actuation modalities under different excitation wavelengths.

Figure 1 depicts a flow diagram of four major steps to exploit RI-insensitive nanolaminated SERS substrates for label-free Raman profiling and classification of living breast cancer and breast normal cells, including (1) SERS substrate fabrication, (2) cell culturing, (3) Raman spectroscopy measurement, and



**Figure 1.** A flow diagram of four major steps to achieve SERS molecular profiling and statistical classification of living breast cancer and breast normal cells using RI-insensitive high-performance nanolaminated SERS substrates. Nanolaminated SERS substrates consist of multistacked vertically oriented nanogap hot spots with large SERS EFs ( $\sim 5 \times 10^7$ ) insensitive to background RI variations (1.30–1.60).

(4) multivariable analysis. As illustrated in Figure 1 (top), nanolaminated SERS substrates consist of multistacked MIM plasmonic nanogaps to support dense hot spots with large SERS EFs ( $>10^7$ ) insensitive to background RI changes. Scalable fabrication (Figure S1, Supporting Information) of nanolaminated SERS substrates with large area ( $\sim 16 \text{ cm}^2$ ) is achieved by soft-lithography molding of polymer nanopillar arrays, physical vapor deposition of alternating Au and  $\text{SiO}_2$  layers, and partial wet-etching of dielectric layers by buffered oxide etchant (BOE) for exposing embedded nanogap hot spots.<sup>37</sup> For the cell culturing step, we employed breast cancer (MDA-MB-231) and breast normal (MCF-10A) cells. We cultured these cells on RI-insensitive nanolaminated SERS substrates without extracellular matrix coating so that SERS signals from hot spots can directly report cell-related molecular information. For label-free SERS measurements, we used a confocal Raman microscope with backscattering configuration. To achieve statistical classification of living breast cancer and breast normal cells by multivariable SERS spectra, we performed multivariate analysis, which involves several critical steps, such as data reduction by principal component analysis (PCA) and predictive classification model construction by supervised linear discriminant analysis (LDA) (details in the Supporting Information).



**Figure 2.** Nanolaminated SERS substrates show RI-insensitive high-performance SERS response. (A) The measured average SERS spectra of BZT for two nanolaminated SERS substrates with 20 and 0 s BOE etching, respectively, and a flat Au film substrate in water (RI = 1.33). The inset shows a schematic illustration of the substrate. The asterisk indicates a Raman shift of  $1071\text{ cm}^{-1}$  which is used for SERS EF calculation. Cross-sectional SEM images of nonetched (top) and 20s-etched (bottom) substrates are shown on the right side. (B) Histograms of SERS intensities and corresponding SERS EFs for the nanolaminated SERS substrate with 20 s BOE etching. The inset is a 2D Raman image of a  $20\text{ }\mu\text{m} \times 20\text{ }\mu\text{m}$  area for the BZT Raman peak at  $1071\text{ cm}^{-1}$ . (C) The measured average SERS spectra of BZT and (D) calculated SERS EFs at different background RIs for the nanolaminated SERS substrate with 20 s BOE etching.

We first assessed the SERS performance of nanolaminated SERS substrates with and without partial wet-etching by measuring Raman spectra of the surface-assembled benzenethiol (BZT) molecules, a nonresonant Raman analyte, in the water environment. Figure 2A shows that the nanolaminated SERS substrate with 20 s wet-etching by BOE can induce 1 order of magnitude higher Raman intensity (e.g., at  $1071\text{ cm}^{-1}$ ) under 2 mW NIR laser excitation ( $785\text{ nm}$ ) than the nonetched one by exposing the embedded nanogap hot spots to molecules in the environment (also shown in their cross-sectional SEM images). In contrast, the flat Au film shows almost no signal even with much higher power (50 mW). Raman spectra in Figure 2A are averaged from 400 pixels within a  $20\text{ }\mu\text{m} \times 20\text{ }\mu\text{m}$  area for different samples. While our previous study shows that 30 s etching time results in the best SERS performance,<sup>37</sup> we use 20 s etching time to trade off slightly reduced SERS sensitivity for improved mechanical robustness of nanolaminated MIM nanostructures during label-free SERS measurements of living cell samples. The inset of Figure 2B shows the 2D confocal Raman image (at  $1071\text{ cm}^{-1}$ ) over a  $20\text{ }\mu\text{m} \times 20\text{ }\mu\text{m}$  area for nanolaminated SERS substrates (etching time of 20 s) in water. To study the uniformity of SERS hot spots on nanolaminated SERS substrates, we also plotted the histograms of  $1071\text{ cm}^{-1}$  Raman signal intensities and corresponding SERS EFs from 1200 pixels acquired from three different areas (Figure 2B), which show a normal distribution of SERS EFs with a peak position adjacent to the mean value and reveal a uniform distribution of hot spots on the SERS substrates. The average SERS EF and relative standard deviation (RSD) over three

spots were calculated to be  $4.9 \times 10^7$  and 16.8%, respectively. The SERS EFs were calculated by the formula  $\text{EF} = (I_{\text{SERS}}/I_{\text{Raman}}) \times (N_{\text{Raman}}/N_{\text{SERS}})$  (details in the Supporting Information).

Next, we studied the RI-dependent SERS performance of nanolaminated SERS substrates with 20 s BOE etching. Figure 2C shows the measured average BZT Raman spectra from 400 pixels over a  $20\text{ }\mu\text{m} \times 20\text{ }\mu\text{m}$  area of the nanolaminated SERS substrates in air and liquids with different RIs from 1.30 to 1.60, which cover RI variations for most intracellular and extracellular components.<sup>35,36</sup> We can observe that the measured BZT Raman spectral profile and peak intensities from nanolaminated SERS substrates do not change much with the change of background RI. For further quantitative analysis, we show the dependence of the average SERS EF values and distribution of hot spots on the background RI values in Figure 2D. As RI increases from 1.30 to 1.60, the average SERS EFs vary between  $5.4 \times 10^7$  and  $3.4 \times 10^7$  in the same order of magnitude. The RSD values of averaged SERS EFs vary between 14.9 and 11.5%. Therefore, RI-insensitive nanolaminated SERS substrates can consistently provide uniform hot spots with large SERS EFs at the interface with cells and cellular networks where local RI values can vary significantly at the subcellular level.

To investigate the physical origin behind the observed RI-insensitive SERS response, we carried out the RI-dependent reflectance measurements of nanolaminated SERS substrates with 20 s BOE etching. As shown in Figure 3A, at the background RI of 1.30, the measured reflectance spectra of nanolaminated SERS substrates exhibit a broadband multi-

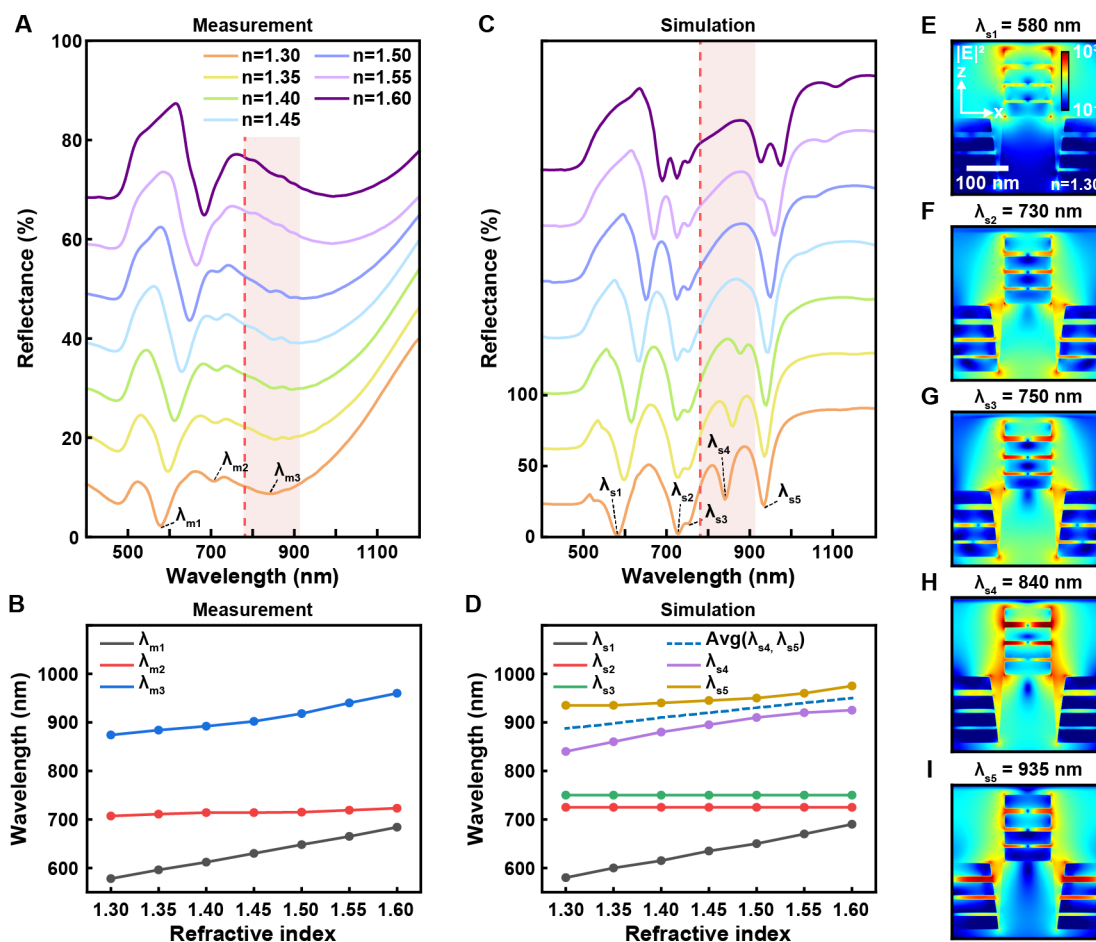


**Figure 3.** Far-field and near-field optical properties of nanolaminated SERS substrates under different background RIs. (A) Measured reflectance spectra of nanolaminated SERS substrates with background RI changing from 1.30 to 1.60 and (B) the dependence of resonant wavelengths of different plasmonic modes on the RI from measurements. (C) FDTD-calculated reflectance spectra of nanolaminated SERS substrates with background RI changing from 1.30 to 1.60 and (D) the dependence of resonant wavelengths of different plasmonic modes on the RI from FDTD calculations. (E–I) The FDTD-calculated  $x$ – $z$  distribution maps of  $|E|^2$  for different plasmonic modes in nanolaminated SERS substrates at a background RI of 1.30.

resonant response featured by a narrow deep reflectance dip at 580 nm ( $\lambda_{m1}$ ), a narrow and shallow reflectance dip at 700 nm ( $\lambda_{m2}$ ), and a broad reflectance dip at 880 nm ( $\lambda_{m3}$ ) covering a very wide spectral range from 700 to 1100 nm. In addition, the RI-insensitive reflectance dip observed below 500 nm is associated with the optical absorption due to the interband electronic transitions in gold. With the background RI increased from 1.30 to 1.60, the narrow  $\lambda_{m1}$  dip and the broad  $\lambda_{m3}$  dip shift a lot from 580 to 690 nm and from 880 to 965 nm, respectively, while the narrow  $\lambda_{m2}$  dip only has a small red-shift from 700 to 715 nm. Figure 3B illustrates the different rates of RI-dependent wavelength shifts for  $\lambda_{m1}$  dip ( $\sim 365$  nm/RIU),  $\lambda_{m2}$  dip ( $\sim 50$  nm/RIU), and  $\lambda_{m3}$  dip ( $\sim 285$  nm/RIU), which reflects that they are associated with different types of plasmonic modes storing different portions of optical energy susceptible to the changes of the background RI. The dashed line and the shaded region in Figure 3A respectively depict the Raman excitation laser wavelength at 785 nm and the associated Raman spectral region up to a Raman shift of  $1800\text{ cm}^{-1}$  ( $\sim 915$  nm in wavelength).

For a better understanding of the multiple resonant features in the reflectance measurements and why they show different RI-dependent behaviors, we used the three-dimensional finite-difference time-domain (FDTD) method (details in the

Supporting Information) to calculate far-field and near-field optical properties of nanolaminated SERS substrates under different background RIs between 1.30 and 1.60 (Figure 3C–I). To model the partially etched plasmonic nanogaps for exposing hot spots to the background environments, we performed FDTD calculations of nanolaminated plasmonic structures with a  $\sim 20$  nm opening depth of background RI in dielectric nanogap layers. At the background RI of 1.30, the FDTD-calculated reflectance spectrum of the nanolaminated sample exhibits five plasmonic resonant dips at 580 nm ( $\lambda_{s1}$ ), 730 nm ( $\lambda_{s2}$ ), 750 nm ( $\lambda_{s3}$ ), 840 nm ( $\lambda_{s4}$ ), and 935 nm ( $\lambda_{s5}$ ) (Figure 3C).

FDTD near-field optical calculations show that the five modes ( $\lambda_{s1}$ ,  $\lambda_{s2}$ ,  $\lambda_{s3}$ ,  $\lambda_{s4}$ , and  $\lambda_{s5}$ ) in nanolaminated plasmonic structures have different mode profiles (Figure 3E–I) and originate from optical hybridization between delocalized plasmonic modes in the constituent MIM nanolaminated nanohole arrays of the bottom part (Supporting Information, Figure S3) and localized plasmonic modes in the constituent MIM nanolaminated nanodisk arrays of the top part (Supporting Information, Figure S4). The  $\lambda_{s1}$  mode results from a mix between background RI-sensitive surface plasmon polariton (SPP)-Bloch waves at the top metal surface of nanolaminated nanohole arrays (Figure S3B) and the back-

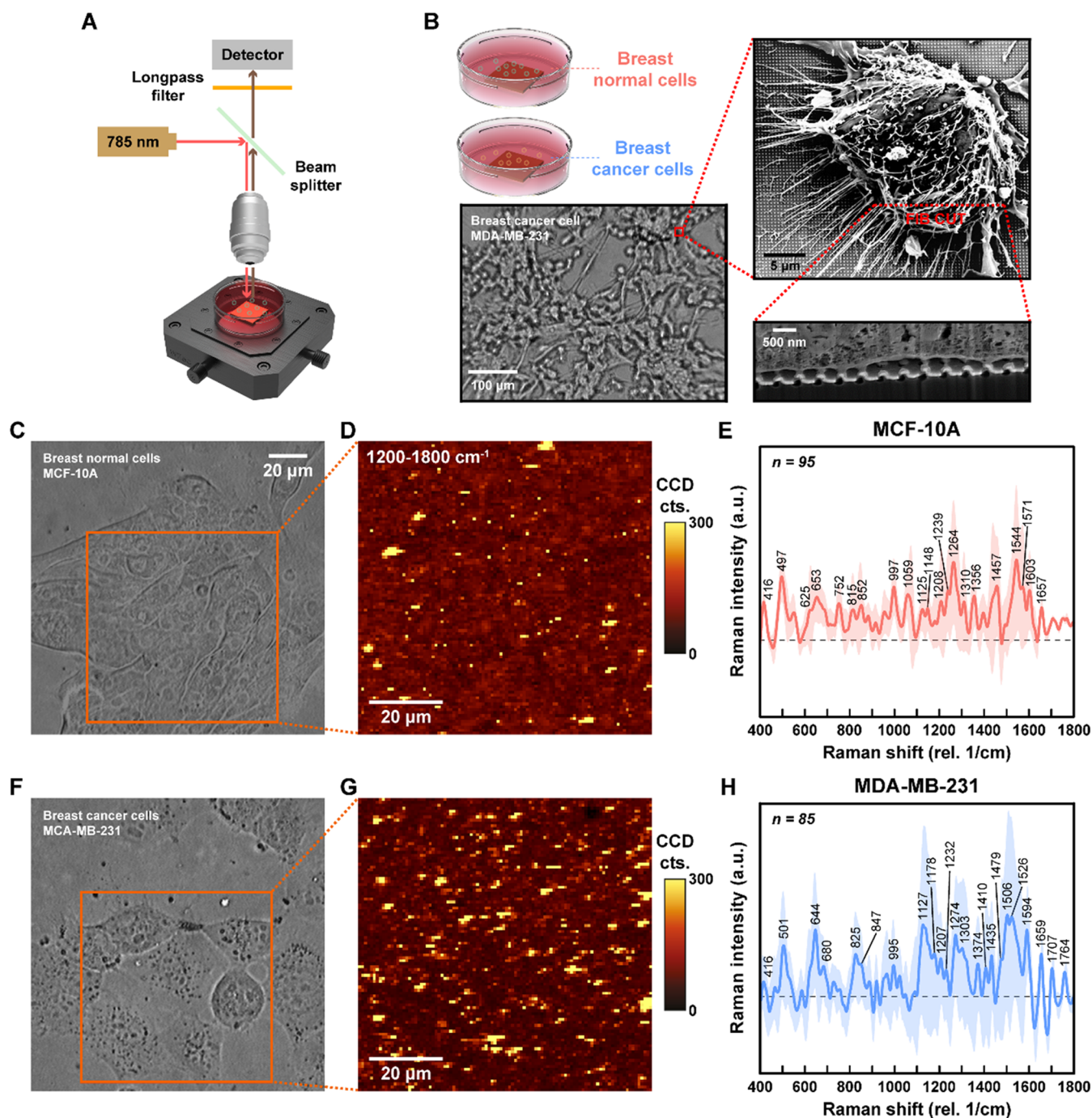


**Figure 4.** Label-free SERS measurements of living breast cancer and normal cells. (A) Schematic illustration of the experimental setup for label-free SERS measurements of cultured living cells. (B) The bright-field image, the top-view SEM image, and the cross-sectional SEM image of cultured breast cancer cells on nanolaminated SERS substrates. (C) Bright-field image, (D) 2D Raman image, and (E) Raman spectra of breast normal cells (MCF-10A) cultured on the SERS substrates. (F) Bright-field image, (G) 2D Raman image, and (H) Raman spectra of breast cancer cells (MCA-MB-231) cultured on the SERS substrates. 2D Raman images for normal and cancer cells (D and G) are plotted using the integrated Raman signals from the protein-related region ( $1200\text{--}1800\text{ cm}^{-1}$ ). The shaded regions in parts E and H illustrate the standard deviations of the averaged SERS spectra for normal and cancer cells.

ground RI-sensitive electric dipole localized surface plasmon (LSP) mode in nanolaminated nanodisks (Figure S4B), and it thus shows a fast RI-dependent wavelength shifting. The two closely spaced  $\lambda_{s2}$  and  $\lambda_{s3}$  modes are mainly associated with background RI-insensitive SPP-Bloch waves at the bottom metal surface of nanolaminated nanohole arrays (Figure S3C,D), and thus, they are not sensitive to background RI changes. The two  $\lambda_{s4}$  and  $\lambda_{s5}$  modes result from the optical

interaction between the background RI-insensitive gap SPP-Bloch waves concentrated in dielectric layers of nanolaminated nanohole arrays (Figure S3E) and the background RI-sensitive magnetic dipole LSP mode supported by nanolaminated nanodisks (Figure S4C). Due to the near-field optical hybridization between localized and delocalized plasmonic modes,<sup>38</sup> as shown in Figure 3D, the resonant wavelengths of  $\lambda_{s4}$  and  $\lambda_{s5}$  modes exhibit an anticrossing behavior with RI

increased from 1.30 to 1.60, in which the low-energy  $\lambda_{s4}$  branch initially red-shifts fast and then is flat-banded while the high-energy  $\lambda_{s5}$  branch behaves in an opposite manner (details in Supporting Information, Figure S5).

By comparing resonant wavelengths of different reflectance dips and their RI-dependent wavelength shifts between measurements (Figure 3A,B) and simulations (Figure 3C,D), the RI-sensitive narrow deep  $\lambda_{m1}$  dip and the RI-insensitive narrow shallow  $\lambda_{m2}$  dip in measurements can be attributed to  $\lambda_{s1}$  and  $\lambda_{s2}/\lambda_{s3}$  modes in simulations, respectively. On the other hand, the RI-sensitive broad  $\lambda_{m3}$  dip in measurements can be associated with the combined optical response of  $\lambda_{s4}$  and  $\lambda_{s5}$  modes in simulations due to their similar resonant wavelengths and similar RI-dependent shifting behaviors (Figure 3B and D). The significant discrepancy of resonant line widths between the broad  $\lambda_{m3}$  dip in measurements and narrower  $\lambda_{s4}/\lambda_{s5}$  modes in simulations is due to a combination of inhomogeneous broadening effects from random geometry variations among unit cell structures and homogeneous broadening effects from significant optical losses associated with metal–dielectric interface roughness.<sup>39</sup> Compared to  $\lambda_{s1}$ ,  $\lambda_{s2}$ , and  $\lambda_{s3}$  modes based on electrical dipole LSP resonances of nanolaminated nanodisks or SPP-Bloch waves at the top/bottom metal surface of nanolaminated nanohole arrays,  $\lambda_{s4}$  and  $\lambda_{s5}$  modes based on magnetic dipole LSP modes in nanolaminated nanodisks and gap SPP-Bloch modes in nanolaminated nanohole arrays can significantly concentrate intense optical fields in dielectric nanogap layers between metal layers and thus are more susceptible to inhomogeneous and homogeneous broadening effects.<sup>39</sup> From FDTD calculations of near-field profiles of the  $\lambda_{s4}$  mode (Figure 3H), SERS EF at vertically oriented nanogap hot spots can be estimated as  $3.0 \times 10^7$  based on the  $|E|^4$  approximation<sup>40</sup> ( $EF \approx |E_{loc}(\omega_o)|^2 \times |E_{loc}(\omega_o - \omega_{vib})|^2$ ) in good agreement with the measured SERS EF of  $5.4 \times 10^7$  (Figure 2D). In sum, experimental and numerical studies reveal that the observed RI-insensitive SERS response is due to the broadband optical response of MIM nanolaminated plasmonic nanostructures by supporting multiple plasmonic modes with highly concentrated optical fields in nanogap hot spots over a wide wavelength range at different background RIs (Figure S6).

As a proof-of-concept demonstration for label-free analysis of living cells, we measured Raman signals from living breast normal (MCF-10A) and cancer (MDA-MB-231) cells cultured on RI-insensitive nanolaminated SERS substrates in four Petri dishes; hence, each dish can be considered as an independent culture environment (details in the Supporting Information). As shown in Figure 4A, a confocal Raman microscope in the backscattering configuration under 785 nm laser excitation is used to measure label-free SERS spectra of living cells (details in the Supporting Information). Based on the cell morphologies of both breast normal and cancer cells (Figure 4B, left bottom, and Figure S7),<sup>41,42</sup> nanolaminated SERS substrates made of Au and SiO<sub>2</sub> appear to be biocompatible for cultured cells. Breast cancer cells exhibit brush-like structures on the cell surface mainly composed of microvilli and cilia with different lengths (top-view SEM image in Figure 4B) in agreement with the previous study.<sup>43</sup> From the cross-sectional SEM image (Figure 4B) by focused ion beam milling, some parts of the cell membrane are found to form intimate adhesion with nanolaminated plasmonic structures containing vertically stacked nanogap hot spots, which can enable direct SERS measurements of molecular environments related to cell

membrane components. Other hot spots without direct adhesion with the cell membrane may also offer cell-related SERS information in terms of secreted metabolites, cell signaling mediators, and exosomes.<sup>44</sup> Therefore, label-free intrinsic Raman signals from plasmonic SERS hot spots could provide biomolecular information related to the cell membrane where the majority of common cancer markers are present.<sup>23,43,45</sup> Parts C and F of Figure 4 show bright-field images of breast normal and cancer cells cultured on the RI-insensitive nanolaminated SERS substrates in regions containing high densities of cells. Parts D and G of Figure 4 show the 2D confocal Raman mapping results over a  $100 \mu\text{m} \times 100 \mu\text{m}$  area for living breast normal and cancer cells by an integration time of 10 ms, where each pixel of a  $1 \mu\text{m} \times 1 \mu\text{m}$  area shows a Raman signal intensity integrated over the protein-related Raman spectral range between 1200 and 1800  $\text{cm}^{-1}$ . Despite the uniform distribution of hot spots on RI-insensitive SERS substrates (Figure 2B), Raman mapping images (Figure 4D and G) from living breast normal and cancer cells exhibit complicated and irregular patterns with heterogeneous distributions of high Raman intensity pixels, which can hardly be correlated to the cell morphology patterns in bright-field microscopy images (Figure 4C and F). This observation reflects that the spatial molecular profiles mapped by uniform SERS hot spots are intrinsically heterogeneous and sporadic for cultured living cells, which can be attributed to the following two facts: (1) extracellular biochemical environment is dynamic and heterogeneous by coupling with complicated biological processes of living cells; (2) surface proteins on the membrane of living cells are sparsely and sporadically distributed, and their positions, configurations, or orientations also change dynamically.<sup>2,5</sup>

To acquire biorelated Raman signals with optimized signal-to-noise ratio, we selected pixels with high Raman signal intensity based on large-area 2D Raman mapping results, and then, we measured the Raman spectrum from these pixels with a longer integration time ( $10 \times 2$  s). To mitigate the potential changes of the biochemical/metabolic status of living cells, Raman measurements for each dish were conducted in less than 2 h once it was taken out from the incubator.<sup>2,46</sup> Moreover, to avoid the potential Raman spectral bias due to adenine-related species generated by living cancer cells in nutrient-deficient environments,<sup>2,46</sup> we did not exchange the culture medium with other solutions such as phosphate-buffered saline (PBS). For each cell type, we obtained  $\sim 90$  Raman spectra from four dishes ( $\sim 20$ – $30$  spectra from each dish). Parts E and H of Figure 4 illustrate the averaged Raman spectra of living breast normal cells and cancer cells with their standard deviations depicted as shaded regions. Some peaks are broader than others due to an ensemble effect arising from contributions of diverse biomolecules within hot spots. Both cases reveal high variations due to different Raman profiles in almost all spectra, reflecting very inhomogeneous chemical constitution of living cells.<sup>2,5</sup> Also, the dish-to-dish difference of culturing environments may contribute to the variations of Raman signals in the measurements.<sup>47</sup>

Compared to breast normal cells, the Raman spectra from breast cancer cells show a large Raman signal variation with a wider shaded region due to higher inherent cancerous heterogeneities. Results for assessing cell viability and comparing major differences between breast normal and cancer cells are summarized in Table S1. Specifically, for both cell types, 2.5 mW of 785 nm did not generate

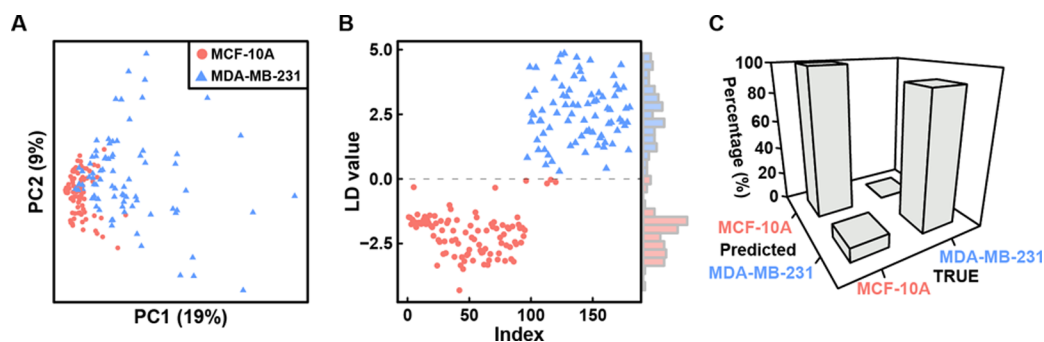


**Figure 5.** Multivariate analysis of living cell SERS for statistical classification of normal and cancer cells. (A) PC score plot and (B) PCA-LDA score plot of living breast normal cells and breast cancer cells. (C) Histograms of confusion matrix for PCA-LDA with LOOCV ( $n = 95$  for MCF-10A and  $n = 85$  for MDA-MB-231).

photoinduced graphitization of organic components of cells, confirmed by the lack of broad D ( $1350\text{ cm}^{-1}$ ) and G ( $1580\text{ cm}^{-1}$ ) bands which can mask small Raman signals from low concentration biomolecules and thus prevent a reliable interpretation. The presence of the DNA backbone peak ( $1125\text{ cm}^{-1}$ ) with simultaneous absence of the adenine ring-breathing mode ( $735\text{ cm}^{-1}$ ) indicates native DNA without denaturing, which also reflects a healthy state of the cells.<sup>48,49</sup> The good viability is further confirmed by the absence of both benzene ring stretching ( $1000\text{ cm}^{-1}$ ) and N–H out-of-plane bending ( $1585\text{ cm}^{-1}$ ), which are related to cellular death dynamics and designated SERS death bands reflecting protein and/or DNA fragments.<sup>50</sup> The presence of cholesterol ( $416\text{ cm}^{-1}$ ) indicates fluidity of the cellular membrane.<sup>49</sup> In terms of lipid regions ( $780\text{--}890$  and  $1400\text{--}1550\text{ cm}^{-1}$ ),<sup>51</sup> cancer cells show higher intensity and number of peaks, suggesting enhanced lipid content from exacerbated synthesis of fatty acid and phospholipids.<sup>52</sup> Unlike normal cells, cancer cells reveal the absence of collagen peaks ( $815$  and  $852\text{ cm}^{-1}$ ), suggesting a dramatic reduction in collagen content in cancerous cells.<sup>53</sup> These lipid and collagen differences are also related to low intensities of proline ( $855\text{ cm}^{-1}$ ) and phospholipid ( $1454\text{ cm}^{-1}$ ) peaks for cancer cells.<sup>54–56</sup> Cancer cells exhibit higher intensities of phenylalanine peaks ( $621$  and  $645\text{ cm}^{-1}$ ) and tyrosine peaks ( $825$ ,  $1164$ , and  $1178\text{ cm}^{-1}$ ) compared to normal cells, reflecting possible elevation in the expression of such aromatic amino acid rich proteins on the cancer cell surface.<sup>52,55</sup> Different protein backbone confirmations—amide I ( $1600\text{--}1800\text{ cm}^{-1}$ ), amide II ( $1480\text{--}1580\text{ cm}^{-1}$ ), and amide III ( $1200\text{--}1350\text{ cm}^{-1}$ )—are also observed.<sup>2,57</sup> The genetic differences could contribute to the different expression of transmembrane proteins. Numerous molecular levels of biological interpretations can be done by side-by-side comparison. However, averaged data obtained from cell population may mask some critical information, particularly the low concentration of biomolecules due to the heterogeneous environment formed by epigenetic variations of chemical composition.<sup>5,47</sup>

Since the label-free intrinsic SERS analysis for living cells provides convoluted Raman signals from molecule ensembles in plasmonic hot spot regions, it is crucial to exploit statistical methods for extraction and analysis of complex multivariable spectroscopic data.<sup>2</sup> In this work, the acquired Raman data from living cells were analyzed by two popular multivariate chemometric techniques, i.e., PCA and LDA, in a hierarchical manner. In particular, we used PCA to reduce the dimensionality of the multivariable data set while retaining

the variance characteristics of the original data set. PCA has been widely used for SERS to visualize statistical segregation of neuronal cell type, proteins, viruses, and bacteria.<sup>18,58–60</sup> The use of PC scores by scatter plots can allow a visual interpretation of the data set variability for determining similarities and differences between cell types (normal and cancer), and PC loadings by vector plots can be used to identify contributions of each wavenumber. Figure 5A shows a PC score plot with overlapped scatters between breast cancer and normal cells, in which cancer cells induce a more extensive spreading of scatters because of their higher intrinsic heterogeneity. Although the lipid- and protein-related peaks are observed in the first two primary PC loadings (Figure S8), these two PCs with a total 28% contribution are insufficient to differentiate between living cancer and normal cells from the inhomogeneous data set. Since PCA does not consider interclass variability, it was used as a data reduction tool to extract significant variables among the data set for subsequent LDA analysis. Before constructing a predictive model, this data reduction step is highly recommended in statistics to avoid poor prediction performance on independent data.<sup>61,62</sup> Unlike PCA, LDA is a supervised technique and the classification criterion is determined by maximized interclass variance (between cell type) and minimized intraclass variance (within each type). The significantly reduced variables (PCs) were used to construct a predictive model by LDA. In our case, we used 38 PCs (95% spectral variance) to build a classification model meeting the requirement of LDA, which is that the number of variables (PCs) should be at least 5 times lower than the number of data (number of spectra = 180).<sup>61</sup> As shown in Figure 5B, the PCA-LDA classification model clearly segregates breast normal cells from breast cancer cells including a more extensive spreading feature of cancer cells by histogram. The prediction ability of the PCA-LDA model was subsequently assessed by leave-one-out cross-validation (LOOCV) using unbiased data. In Figure 5C, the classification result is shown in a confusion matrix form with an overall accuracy of 96% (MCF-10A, 100%; MDA-MB-231, 91%). A confusion matrix with raw number of spectra is described in Table S2.

In summary, we have demonstrated RI-insensitive high-performance nanolaminated SERS substrates, which show a uniform distribution of SERS EF ( $5 \times 10^7$ ) at different background RIs ranging from 1.30 to 1.60. Such nanolaminated SERS substrates can be manufactured in a scalable, high-throughput, and inexpensive manner desirable for disposable biochemical analysis applications. To understand

broadband multiresonant optical properties responsible for the RI-insensitive SERS response, we measured and simulated far-/near-field optical properties of the SERS substrates with physical interpretation for microscopic origins of different plasmonic modes. As a proof-of-concept demonstration, we employed the RI-insensitive nanolaminated SERS substrates for molecular profiling and statistical classification of in vitro living breast normal and cancer cells with an accuracy of 96%. Compared to conventional single-resonant SERS substrates, multiresonant nanolaminated SERS substrates in this work have several advantages: (1) uniform hot spots with consistently high SERS EFs insensitive to background local RI variations in complex biological systems; (2) good fabrication scalability for mass production of large-area SERS substrates, suitable for real-time biochemical analysis of living cell cultures; (3) wavelength-multiplexed optical multimodality at the nano–bio interface. Therefore, we envision that RI-insensitive high-performance nanolaminated SERS substrates can enable a real-time, label-free, and highly sensitive biochemical analysis not only for living cancer cell diagnostic applications but also for fundamental biological study to investigate spatiotemporal biochemical dynamics in cellular networks.

## ■ ASSOCIATED CONTENT

### Supporting Information

The Supporting Information is available free of charge on the ACS Publications website at DOI: [10.1021/acs.nanolett.9b02864](https://doi.org/10.1021/acs.nanolett.9b02864).

Cell culture; experimental setup; multivariate analysis; 3D FDTD simulation; SERS EF calculation; fabrication details with SEM images; far-/near-field optical properties of nanolaminated nanohole and nanodisk arrays; anticrossing behavior; near-field optical properties at 785 nm; MCF-10A bright-field image; PC loading plots; Raman peaks; confusion matrix with raw number of spectra (PDF)

## ■ AUTHOR INFORMATION

### Corresponding Author

\*E-mail: [wzh@vt.edu](mailto:wzh@vt.edu).

### ORCID

Wonil Nam: 0000-0002-7804-3049

Xiang Ren: 0000-0002-8882-6362

Wei Zhou: 0000-0002-5257-3885

### Notes

The authors declare no competing financial interest.

## ■ ACKNOWLEDGMENTS

This work was supported by AFOSR Young Investigator Award FA9550-18-1-0328.

## ■ REFERENCES

- (1) Kneipp, J.; Kneipp, H.; Kneipp, K. *Chem. Soc. Rev.* **2008**, *37* (5), 1052–1060.
- (2) Zong, C.; Xu, M.; Xu, L. J.; Wei, T.; Ma, X.; Zheng, X. S.; Hu, R.; Ren, B. *Chem. Rev.* **2018**, *118* (10), 4946–4980.
- (3) Nie, S. M.; Emery, S. R. *Science* **1997**, *275* (5303), 1102–1106.
- (4) Ding, S.-Y.; Yi, J.; Li, J.-F.; Ren, B.; Wu, D.-Y.; Panneerselvam, R.; Tian, Z.-Q. *Nat. Rev. Mater.* **2016**, *1* (6), 16021.
- (5) Kuku, G.; Altunbek, M.; Culha, M. *Anal. Chem.* **2017**, *89* (21), 11160–11166.

(6) Zheng, X. S.; Jahn, I. J.; Weber, K.; Cialla-May, D.; Popp, J. *Spectrochim. Acta, Part A* **2018**, *197*, 56–77.

(7) Qian, X.; Peng, X. H.; Ansari, D. O.; Yin-Goen, Q.; Chen, G. Z.; Shin, D. M.; Yang, L.; Young, A. N.; Wang, M. D.; Nie, S. *Nat. Biotechnol.* **2008**, *26* (1), 83–90.

(8) van Lierop, D.; Faulds, K.; Graham, D. *Anal. Chem.* **2011**, *83* (15), 5817–21.

(9) Robson, A. F.; Hupp, T. R.; Lickiss, F.; Ball, K. L.; Faulds, K.; Graham, D. *Proc. Natl. Acad. Sci. U. S. A.* **2012**, *109* (21), 8073–8.

(10) Lin, L.; Tian, X. D.; Hong, S. L.; Dai, P.; You, Q. C.; Wang, R. Y.; Feng, L. S.; Xie, C.; Tian, Z. Q.; Chen, X. *Angew. Chem., Int. Ed.* **2013**, *52* (28), 7266–7271.

(11) Song, Z. L.; Chen, Z.; Bian, X.; Zhou, L. Y.; Ding, D.; Liang, H.; Zou, Y. X.; Wang, S. S.; Chen, L.; Yang, C.; Zhang, X. B.; Tan, W. H. *J. Am. Chem. Soc.* **2014**, *136* (39), 13558–13561.

(12) Kang, J. W.; So, P. T.; Dasari, R. R.; Lim, D. K. *Nano Lett.* **2015**, *15* (3), 1766–72.

(13) Hu, S.; Liu, B. J.; Feng, J. M.; Zong, C.; Lin, K. Q.; Wang, X.; Wu, D. Y.; Ren, B. *J. Am. Chem. Soc.* **2018**, *140* (42), 13680–13686.

(14) Xu, M.; Ma, X.; Wei, T.; Lu, Z. X.; Ren, B. *Anal. Chem.* **2018**, *90* (23), 13922–13928.

(15) Dijkstra, R. J.; Scheenen, W. J.; Dam, N.; Roubos, E. W.; ter Meulen, J. J. *Neurosci. Methods* **2007**, *159* (1), 43–50.

(16) Ando, J.; Fujita, K.; Smith, N. I.; Kawata, S. *Nano Lett.* **2011**, *11* (12), 5344–8.

(17) Yang, J.; Cui, Y.; Zong, S.; Zhang, R.; Song, C.; Wang, Z. *Mol. Pharmaceutics* **2012**, *9* (4), 842–9.

(18) Huefner, A.; Kuan, W. L.; Barker, R. A.; Mahajan, S. *Nano Lett.* **2013**, *13* (6), 2463–70.

(19) Han, G.; Liu, R.; Han, M. Y.; Jiang, C.; Wang, J.; Du, S.; Liu, B.; Zhang, Z. *Anal. Chem.* **2014**, *86* (23), 11503–7.

(20) Kang, B.; Austin, L. A.; El-Sayed, M. A. *ACS Nano* **2014**, *8* (5), 4883–4892.

(21) Huefner, A.; Kuan, W. L.; Muller, K. H.; Skepper, J. N.; Barker, R. A.; Mahajan, S. *ACS Nano* **2016**, *10* (1), 307–16.

(22) Xu, L.; Kuang, H.; Xu, C.; Ma, W.; Wang, L.; Kotov, N. A. *J. Am. Chem. Soc.* **2012**, *134* (3), 1699–709.

(23) Yan, B.; Reinhard, B. M. *J. Phys. Chem. Lett.* **2010**, *1* (10), 1595–1598.

(24) Huang, J. Y.; Zong, C.; Xu, L. J.; Cui, Y.; Ren, B. *Chem. Commun. (Cambridge, U. K.)* **2011**, *47* (20), 5738–40.

(25) Jiang, X.; Jiang, Z.; Xu, T.; Su, S.; Zhong, Y.; Peng, F.; Su, Y.; He, Y. *Anal. Chem.* **2013**, *85* (5), 2809–16.

(26) El-Said, W. A.; Kim, S. U.; Choi, J.-W. *J. Mater. Chem. C* **2015**, *3* (16), 3848–3859.

(27) Albanese, A.; Chan, W. C. W. *ACS Nano* **2011**, *5* (7), 5478–5489.

(28) Khlebtsov, N.; Dykman, L. *Chem. Soc. Rev.* **2011**, *40* (3), 1647–1671.

(29) Caprettini, V.; Huang, J. A.; Moia, F.; Jacassi, A.; Gonano, C. A.; Maccaferri, N.; Capozza, R.; Dipalo, M.; De Angelis, F. *Adv. Sci. (Weinh)* **2018**, *5* (12), 1800560.

(30) Liang, O.; Wang, P.; Xia, M.; Augello, C.; Yang, F.; Niu, G.; Liu, H.; Xie, Y. H. *Biosens. Bioelectron.* **2018**, *118*, 108–114.

(31) Jung, K.; Hahn, J.; In, S.; Bae, Y.; Lee, H.; Pikhitsa, P. V.; Ahn, K.; Ha, K.; Lee, J. K.; Park, N.; Choi, M. *Adv. Mater.* **2014**, *26* (34), 5924–9.

(32) Zhang, X.; Zheng, Y.; Liu, X.; Lu, W.; Dai, J.; Lei, D. Y.; MacFarlane, D. R. *Adv. Mater.* **2015**, *27* (6), 1090–6.

(33) Kanipe, K. N.; Chidester, P. P.; Stucky, G. D.; Moskovits, M. *ACS Nano* **2016**, *10* (8), 7566–71.

(34) Liu, B.; Yao, X.; Chen, S.; Lin, H.; Yang, Z.; Liu, S.; Ren, B. *Adv. Funct. Mater.* **2018**, *28* (43), 1802263.

(35) Liu, P. Y.; Chin, L. K.; Ser, W.; Chen, H. F.; Hsieh, C. M.; Lee, C. H.; Sung, K. B.; Ayi, T. C.; Yap, P. H.; Liedberg, B.; Wang, K.; Bourouina, T.; Leprince-Wang, Y. *Lab Chip* **2016**, *16* (4), 634–44.

(36) Zhang, Q.; Zhong, L.; Tang, P.; Yuan, Y.; Liu, S.; Tian, J.; Lu, X. *Sci. Rep.* **2017**, *7* (1), 2532.

- (37) Song, J.; Nam, W.; Zhou, W. *Advanced Materials Technologies* **2019**, *4*, 1800689.
- (38) Zhou, W.; Suh, J. Y.; Hua, Y.; Odom, T. W. *J. Phys. Chem. C* **2013**, *117* (6), 2541–2546.
- (39) Song, J.; Zhou, W. *Nano Lett.* **2018**, *18* (7), 4409–4416.
- (40) Ding, S. Y.; You, E. M.; Tian, Z. Q.; Moskovits, M. *Chem. Soc. Rev.* **2017**, *46* (13), 4042–4076.
- (41) Hardy, S.; Langelier, Y.; Prentki, M. *Cancer Res.* **2000**, *60* (22), 6353–6358.
- (42) Debnath, J.; Muthuswamy, S. K.; Brugge, J. S. *Methods* **2003**, *30* (3), 256–268.
- (43) Iyer, S.; Gaikwad, R. M.; Subba-Rao, V.; Woodworth, C. D.; Sokolov, I. *Nat. Nanotechnol.* **2009**, *4* (6), 389–93.
- (44) Gangoda, L.; Liem, M.; Ang, C. S.; Keerthikumar, S.; Adda, C. G.; Parker, B. S.; Mathivanan, S. *Proteomics* **2017**, *17* (23–24), 1600370.
- (45) Dube, D. H.; Bertozzi, C. R. *Nat. Rev. Drug Discovery* **2005**, *4* (6), 477–488.
- (46) Ozaki, Y.; Kneipp, K.; Aroca, R. *Frontiers of Surface-Enhanced Raman Scattering: Single Nanoparticles and Single Cells*; John Wiley & Sons: Hoboken, NJ, 2014.
- (47) Altschuler, S. J.; Wu, L. F. *Cell* **2010**, *141* (4), 559–63.
- (48) Kneipp, K.; Haka, A. S.; Kneipp, H.; Badizadegan, K.; Yoshizawa, N.; Boone, C.; Shafer-Peltier, K. E.; Motz, J. T.; Dasari, R. R.; Feld, M. S. *Appl. Spectrosc.* **2002**, *56* (2), 150–154.
- (49) La Rocca, R.; Messina, G. C.; Dipalo, M.; Shalabaeva, V.; De Angelis, F. *Small* **2015**, *11* (36), 4632–7.
- (50) Austin, L. A.; Kang, B.; El-Sayed, M. A. *J. Am. Chem. Soc.* **2013**, *135* (12), 4688–91.
- (51) Krafft, C.; Neudert, L.; Simat, T.; Salzer, R. *Spectrochim. Acta, Part A* **2005**, *61* (7), 1529–35.
- (52) Bi, X.; Rexer, B.; Arteaga, C. L.; Guo, M.; Mahadevan-Jansen, A. *J. Biomed. Opt.* **2014**, *19* (2), No. 025001.
- (53) Manciu, F. S.; Ciubuc, J. D.; Parra, K.; Manciu, M.; Bennet, K. E.; Valenzuela, P.; Sundin, E. M.; Durrer, W. G.; Reza, L.; Francia, G. *Technol. Cancer Res. Treat.* **2017**, *16* (4), 461–469.
- (54) Huang, Z.; McWilliams, A.; Lui, H.; McLean, D. I.; Lam, S.; Zeng, H. *Int. J. Cancer* **2003**, *107* (6), 1047–52.
- (55) Movasaghi, Z.; Rehman, S.; Rehman, I. U. *Appl. Spectrosc. Rev.* **2007**, *42* (5), 493–541.
- (56) Auner, G. W.; Koya, S. K.; Huang, C.; Broadbent, B.; Trexler, M.; Auner, Z.; Elias, A.; Mehne, K. C.; Brusatori, M. A. *Cancer Metastasis Rev.* **2018**, *37* (4), 691–717.
- (57) Rygula, A.; Majzner, K.; Marzec, K. M.; Kaczor, A.; Pilarczyk, M.; Baranska, M. *J. Raman Spectrosc.* **2013**, *44* (8), 1061–1076.
- (58) Abell, J. L.; Driskell, J. D.; Dluhy, R. A.; Tripp, R. A.; Zhao, Y. P. *Biosens. Bioelectron.* **2009**, *24* (12), 3663–70.
- (59) Das, G.; Gentile, F.; Coluccio, M. L.; Perri, A. M.; Nicastri, A.; Mecarini, F.; Cojoc, G.; Candeloro, P.; Liberale, C.; De Angelis, F.; Di Fabrizio, E. *J. Mol. Struct.* **2011**, *993* (1–3), 500–505.
- (60) Zhang, L.; Xu, J.; Mi, L.; Gong, H.; Jiang, S.; Yu, Q. *Biosens. Bioelectron.* **2012**, *31* (1), 130–6.
- (61) Martin, F. L.; Kelly, J. G.; Llabjani, V.; Martin-Hirsch, P. L.; Patel, I. I.; Trevisan, J.; Fullwood, N. J.; Walsh, M. J. *Nat. Protoc.* **2010**, *5* (11), 1748–60.
- (62) Kelly, J. G.; Trevisan, J. I.; Scott, A. D.; Carmichael, P. L.; Pollock, H. M.; Martin-Hirsch, P. L.; Martin, F. L. *J. Proteome Res.* **2011**, *10* (4), 1437–1448.